Determining rheology from deformation data: The case of central Italy

Michele M.C. Carafa and Salvatore Barba
(michele.carafa@ingv.it; salvatore.barba@ingv.it)
Istituto Nazionale di Geofisica e Vulcanologia, Roma, Italy

Revised text, 23 October 2010

Determining rheology from deformation data: The case of central Italy

Michele M.C. Carafa and Salvatore Barba
(michele.carafa@ingv.it; salvatore.barba@ingv.it)
Istituto Nazionale di Geofisica e Vulcanologia, Roma, Italy

Abstract

The study of geodynamics relies on an understanding of the strength of the lithosphere. However, our knowledge of kilometer-scale rheology has generally been obtained from centimeter-sized laboratory samples or from microstructural studies of naturally deformed rocks. In this study, we present a method that allows rheological examination at a larger scale. Utilizing forward numerical modeling, we simulated lithospheric deformation as a function of heat flow and rheological parameters and computed several testable predictions including horizontal velocities, stress directions, and the tectonic regime. To select the best solutions, we compared the model predictions with experimental data. We applied this method in Italy and found that the rheology shows significant variations at small distances. The strength ranged from 0.6±0.2 TN/m within the Apennines belt to 21±6 TN/m in the external Adriatic thrust. These strength values correspond to an aseismic mantle in the upper plate and to a strong mantle within the Adriatic lithosphere, respectively. With respect to the internal thrust, we found that strike-slip or transpressive, but not compressive, earthquakes can occur along the deeper portion of the thrust. The differences in the lithospheric strength are greater than our estimated uncertainties and occur across the Adriatic subduction margin. Using the proposed method, the lithospheric strength can be also determined when information at depth is scarce but sufficient surface data are available.

Index terms: 8002 Continental neotectonics; 8163 Rheology and friction of fault zones; 8031 Rheology: crust and lithosphere; 8020 Mechanics, theory and modeling.

1. Introduction

The strength of the lithosphere has an important influence on a number of geodynamic problems, including the bending of the lithosphere and its gravitational collapse (Bodine et al., 1981; Rey et al., 2001). One-dimensional lithospheric strength is usually represented by a diagram of shear stress versus depth (Brace and Kohlstedt, 1980) and strongly depends on the km-scale rheology of the constituent rocks. This influential but poorly understood constitutive property is usually extrapolated from cm-sized laboratory samples (Hirth and Kohlstedt, 2003; Zhang and Karato, 1995), from structural studies of naturally deformed rocks (Twiss, 1977; Tullis, 2002; Evans, 2005), or from a larger-scale perspective (Sibson et al., 1979; Thatcher, 1983; Bird, 1994; Pollitz et al., 2000; Handy, 2004; Thatcher, 2009).

Assessing the rheological properties of rocks for the broad range of thermodynamic conditions that exist in the lithosphere remains a daunting task. Rock rheology depends on the mineralogy, fluid content, mineral grain size, temperature, pressure, and deformation history of the material (Karato, 2008). This information is very difficult to determine at depth; as a result, a variety of rheological models have been developed. For several years, lithosphere deformation has mainly been described by a model consisting of a weak lower crust between a relatively strong upper crust and uppermost mantle (Brace and Kohlstedt 1980; Zoback and Townend 2001; Burov and Watts, 2006). Following Jackson (2002), we will refer to such a model as the "jelly-sandwich model". Jackson (2002) alternatively proposed a model with a weak mantle and a relatively strong lower crust in which the strength of the lithosphere is carried mainly by the brittle crust; we call this the "crème-brulée model" after Burov and Watts (2006). A third model, named "banana split", has been proposed in high-deformation zones where processes such as shear heating, grain-size reduction, chemical alteration, and phase changes weaken the major lithospheric faults, resulting in very low shear stress values (Burgmann and Dresen, 2008). These models differ in the integrated strength and shear-stress envelopes they posit and represent different views of the rheological properties of the lithosphere.

Knowing the rheology and the strength of the lithosphere gives us insight into the spatial and frequency-size distributions of the seismicity (Lamontagne and Ranalli, 1996; Doglioni et al., 2010). An intriguing key point is the definition of the relationships among the strength of the lithosphere, the rheological parameters, the stress-axis orientation, and the strain-rate magnitudes. Gross rheological characteristics for the western United States were obtained by Flesh et al. (2000) using the magnitude of the strain-rate tensor and the magnitude of the total deviatoric stress tensor. Alternatively, Zoback and Townend (2001) assumed the strength of the lithosphere to be 3 TN/m and estimated the average strain rate of the intraplate lithosphere by varying heat flow, conductivity, heat productivity, and rheological parameters using a Monte Carlo technique. A similar approach was followed by Zoback et al. (2002) in constructing their "steady-state failure equilibrium" model, which was able to provide a first-order constraint on the rate of lithosphere deformation. More recently, GPS and/or stress-data inversion procedures have been used by Becker et al. (2005), Townend and Zoback (2006), and Keiding et al. (2009) to study the deformation field within the elastic regime. Here, we present a method for use in lithosphere-rheology studies. By means of forward numerical modeling, we tested different rheological behaviors to compute the strength of the lithosphere and the shear-stress distribution at depth. We applied this method in central Italy and used several datasets (stress orientations, focal mechanisms, and GPS measurements) to select the best set that were of rheological parameters.

Across the margin of the continental subduction in Italy, we found a sharp variation in the strength of the lithosphere; the upper plate region showed a weak mantle, which is a "crème-brulée"-like behavior, whereas the forearc showed higher strength, especially in the lithospheric mantle. Our approach thus reduces the uncertainty in the choice of laboratory flow laws and complements field work.

2. Study area and data

The Apennines are a fold-and-thrust seismic belt that represents the NW-SE trending extensional boundary between the continental Adriatic microplate to the NE and the young Tyrrhenian crust to the SW (Figure 1). Along the axis of the belt, large normal faults overlie compressional structures, a feature that is interpreted as the back-arc extension of the west-directed Adriatic subduction (Doglioni, 1998). Compressional features are present to the east, toward the Adriatic Sea. The thrust system progressively migrates eastward (Pialli et al., 1998; Doglioni et al., 1999) and shows tectonic activity in the Holocene from the Po Plain (Vannoli et al., 2004) to the Mid-Adriatic Ridge (Scrocca et al., 2007). To the west toward the Tyrrhenian Sea, the extension has been accompanied since the Miocene by a thinning of the earth's crust, volcanic activity, and high heat flows (Pialli et al., 1998, and references therein).

In the first stage of this work, we analyzed the results from a large-scale model that includes Italy and its surroundings (inset of Figure 1). We then focused on the east side of the Central Apennines, which we further divided into three areas of different tectonic behavior (extension, intermediate, and compression). We utilized two datasets: S_{Hmax} orientations from the World Stress Map database (Heidbach et al., 2008) and GPS data (Devoti et al., 2010). In the following discussion, we first describe the data at the model scale and then in detail for the central Apennines.

The World Stress Map database includes 352 borehole breakouts (238 with A-, B-, and C-quality; Heidbach et al., 2008), 1023 earthquake-fault-plane solutions (all of B and C quality, M>4.0), two formal inversions of earthquake focal mechanisms (B quality), and 14 fault data of C quality in the model area. The stress data clearly identify the existence of an extension perpendicular to the axis of the Apennines and compression perpendicular to the Southern Alps and the thrust of Northern Apennines, as also shown by Meletti et al. (2008).

The horizontal velocities in Italy were derived from the analysis of continuous GPS observations collected between 1998 and 2009 (Devoti et al., 2010). The time series are specified with respect to the ITRF2005 and the Eurasian Plate. The complete GPS velocity field is derived from a distributed-session approach and shows a standard deviation of ~0.5 mm/yr. The geodetic strain rates indicate extension along the Apennines of 50–80x10^{-9} yr^{-1} and areas of compressive tectonics of 30–50x10^{-9} yr^{-1}. The GPS kinematic description of the crustal deformation shows a high coherence with the seismotectonic setting of the Italian area.

We considered the east side of the Central Apennines as being divided into three areas of different tectonics. Listed from the axis belt to the east (Figure 1), these are the extensional belt axis (EX), the deep internal thrust (IT), and the external thrust (ET). In the EX, the orientation of S_{Hmax} is mostly NW–SE. The tectonic regime can be inferred by earthquake focal mechanisms (Frepoli and Amato, 1997), quaternary fault-slip data (Boncio et al., 2004), stress data, and morphotectonic and paleoseismological data (Michetti et al., 1996). The velocity field obtained from continuous GPS data also shows extension between the western and eastern sides of the Apennines (Devoti et al., 2008). The western boundary of the EX region coincides with the surface projection of an active, regional-scale, east-dipping, low-angle, extensional detachment fault (see Boncio and Lavecchia, 2000). The following values of filtered surface heat flow have been reported in the literature, with a variability of ca. 20 mW/m^2: 65–75 mW/m^2 (Della Vedova et al., 2001), 50–80 mW/m^2 (Pasquale et al., 1997), and 60–80 mW/m^2 (Pauselli and Federico, 2002).

The IT region is situated between the Apennines and the coastal Adriatic zone. The few available focal mechanisms are normal at shallow depths and transpressive at greater depths (~17–25 km). Negredo et al. (1999) proposed that the tectonic regime in this area changes with depth; the deeper sedimentary layers are undergoing flexure and contraction while the shallower sedimentary layers are undergoing extension, with the transition located at a depth of ~15–18 km. The complexity of the IT requires modeling of the deeper sedimentary layer, the top of which is located at ~18 km. The heat-flow density in the IT is lower than that in the EX, with estimates ranging from 40 mW/m^2 (Pasquale et al., 1997) to 45–60 mW/m^2 (Pauselli and Federico, 2002) or 50–75 mW/m^2 (Della Vedova et al., 2001).

Along the external thrust (ET), morphotectonic analyses indicate Holocene activity (Vannoli et al., 2004), whereas the offshore direction of S_{Hmax}, being mainly arc-perpendicular, shows no dominant orientation and cannot be related to a simple rotation of the Adriatic microplate (Barba et al., 2008). Based on a statistical analysis of the migration and shortening rates of the folds and thrusts, Basili and Barba (2007) reported the activity of the easternmost anticlines, both onshore and offshore. Through an analysis of several seismic profiles, Scrocca et al. (2009) confirmed that the shallowest sediments are deformed and dislocated by compression. Shortening rates of up to 3 mm/yr were identified (Lavecchia et al., 1994; Scrocca et al., 2007; Basili and Barba, 2007). Geodetic analyses, however, are not yet suitable for the study of compression because of the paucity of onshore sites (D’Agostino et al., 2008) and must instead rely on distant GPS sites, which are located along the Dinarides (as in Caporali, 2009, DPC-S1). The lithosphere in the ET is cold, and the heat-flow density is ~40 mW/m^2 (Pauselli and Federico, 2002) with the highest values (40–65 mW/m^2) proposed by Della Vedova et al. (2001).

The amount and type of available data for the model area and for each of the three individual regions, with corresponding values and ranges, are listed in Table 1.

3. Method

We studied the strength of the lithosphere using a trial-and-error procedure (Figure 2) that minimizes the deviations of the model predictions from surface data. Using the finite-element code SHELLS (Kong and Bird, 1995; Bird, 1999), we performed several numerical experiments in which the heat flows, the rheological parameters, and the magnitudes of the basal shear tractions were varied to compute testable predictions of several parameters such as horizontal velocities, S_{Hmax} directions, and tectonic regimes. We performed this modeling in two steps. We first modeled the data over the whole Italian region (inset of Figure 1) and then considered only the stress data in central Italy (Table 1). We selected a set of the best models as determined by their fit to independent datasets of observations from Italy. For each numerical experiment i, we determined the shear stress $\tau_s^i(z)$ at depth and the integrated strength $\Sigma_i = \int \tau_s^i(z)\, dz$, and we averaged these quantities over the set of best models.

The method we devised has several advantages. The two-step approach allows for the calculation of detailed results in small areas while maintaining results that are reliable at a larger scale. The use of independent datasets helps to reduce systematic error and is useful in estimating the extent of random error. Averaging over the best models reduces the dependence on measurement errors and provides more robust results.

3.1. Model setup and boundary conditions

We used the thin-shell finite-element code SHELLS (Bird, 1999), which allows faults, topography, and rheology to be incorporated into a laterally varying crustal structure. The model covers the entire area of Italy (inset of Figure 1) and adopts the same mesh as that used by Barba et al. (2008; 2010). Our grid consists of 5126 triangular continuum elements and 822 fault elements. The model is composed of two layers (crust and mantle) of variable thickness plus topography. Temperature and strength are depth-dependent, as is the shear-stress tensor. Physical and rheological parameters do not vary laterally but do vary from the crust to the mantle (Table 2). We derived the crust and lithosphere thicknesses from the literature (Nicolich, 2001; Marone et al., 2003; Calcagnile and Panza, 1981; Babuska and Plomerova, 2006). For the faults, we adopted the composite seismogenic sources from DISS v.3.0.2 (DISS Working Group, 2006; Basili et al., 2008), i.e., source models that incorporate one or more seismogenic faults with similar parameterizations in the same source and are not segmented. We also incorporated active faults that are not included in the DISS database, such as those from Papanikolaou and Roberts (2007), and those that were included in later versions of the database, such as the Apennine external thrusts (Scrocca et al., 2007).

The boundary conditions were set in the Eurasian reference frame and were the same for all experiments. These conditions show the best fit with the data in Barba et al. (2008; 2010). At the southern edge (the AF and IO borders in Figure 1), we applied the Eurasia-Nubia convergence condition (Serpelloni et al., 2007); thus, the “TR” edges were subjected to reflection symmetry across the North–AF thrust. All of the “EU” edges are fixed with respect to Eurasia. For the “AD” edge, we set the edge-orthogonal velocities to zero while the edge-parallel components were left free.

Basal shear tractions directed towards the northeast were applied below the Apennines (see dashed areas, inset of Figure 1) at a depth of 400 km with uniform magnitude. In the horizontal plane, these tractions are translated by means of simple shear into tractions at the base of the model lithosphere through the assumed rheology (see Bird et al., 2006). Here, the magnitude of the basal shear tractions plays the role of a single free parameter (see below) and ranges from 15 to 50 MPa.

3.2. Free parameters

We considered the heat flows, the rheological parameters, and the magnitudes of basal shear tractions as free parameters. We explored the range of uncertainty in each parameter by a trial-and-error procedure with discrete sampling steps (Table 2).

Each combination of heat flow (q_{EX}, q_{IT}, and q_{ET}), set of rheological parameters (R1-4), and magnitude of basal shear tractions (Φ) constitutes an independent simulation. For each combination, the model predictions were computed with the SHELLS finite-element code (Bird, 1999).

In exploring the range of heat-flow values for each of the three studied areas (EX, IT, and ET), we assigned a single uniform value (q_{EX}, q_{IT}, and q_{ET}, respectively) to represent the average heat flow in all elements within each area. Outside of these areas, the steady-state heat-flow density was derived from the literature (Pasquale et al., 1997, 1999; Verdoya et al., 2005).

We defined four different sets of rheological parameters (R1–R4 in Table 2) that represent distinct and possible behaviors of the lithosphere within the study region. These parameters correspond to the different strengths of the lithosphere. The parameters R1 to R4 (Table 2) are listed in order of increasing strength Σ and deepening brittle-ductile transition, from more ductile to stronger and more brittle, for both the crust and mantle. Among the laboratory rheological parameters, our choices range approximately from Westerly granite wet (R1) to anorthosite (R4) for the crust and from plagioclase (R1) to olivine (R4) for the mantle (Watts, 2001; Burgmann and Dresen, 2008). Each set includes crust and mantle parameters and is uniform over the entire model.

We applied northeastward basal shear tractions Φ under the Apennines in the range of 15–50 MPa to represent the mantle flow–lithosphere interactions (Doglioni, 1987). This range of basal tractions corresponds to a shortening of 0.1-3 mm/yr across the Apennines external thrust (Barba et al., 2008) and thus accounts for the shortening reported in the literature (Lavecchia, 1994; Vannoli et al., 2004). Basal shear tractions are considered here as a discrete random variable; they contribute to the final uncertainties and are not further discussed herein.

3.3. Rheological modeling

The critical value of the shear stress $\tau_s(z)$ (above which failure of the lithosphere occurs) is defined as the least of three upper limits, i.e.,

$$\tau_s = min\left(\tau_s^{fric}, \tau_s^{creep}, \tau_s^{plast}\right)$$

given by empirical relations for brittle frictional sliding, dislocation creep, and plastic deformation (Bird, 1989; 1999). For frictional sliding, we have the following:

$$\tau_s^{fric}(z) = g \cdot z \cdot \left(\rho_{litho} - \lambda \cdot \rho_{H_2O}\right) \cdot \delta = \rho_{litho} \cdot g \cdot z \cdot (1 - \lambda')$$

where z is the depth, g is gravitational acceleration, ρ_{litho} is the density of the crust or mantle, ρ_{H_2O} is the mean density of water, λ is the efficacy of the pore pressure, λ' is the pore-fluid factor, and

$$\delta = \begin{cases} \dfrac{\gamma-1}{2\gamma} & (\text{extension};\ \dot{e}_1 = 0) \\ \dfrac{\gamma-1}{2} & (\text{compression};\ \dot{e}_2 = 0) \\ \omega + \left[\dfrac{\gamma-1}{2\gamma} - \omega\right] \cdot \left|\sin\left(2 \cdot tan^{-1}\dfrac{\dot{e}_2}{|\dot{e}_1|} - \frac{\pi}{2}\right)\right| & (\text{transtension};\ |\dot{e}_1| < \dot{e}_2) \\ \omega + \left[\dfrac{\gamma-1}{2} - \omega\right] \cdot \left|\sin\left(2 \cdot tan^{-1}\dfrac{\dot{e}_2}{|\dot{e}_1|} - \frac{\pi}{2}\right)\right| & (\text{transpression};\ |\dot{e}_1| > \dot{e}_2) \end{cases}$$

$$\omega = sin(tan^{-1}\mu)$$
$$\gamma = \frac{1+\omega}{1-\omega}$$

where μ is the coefficient of friction of the continuum and $\dot{e}_1$ and $\dot{e}_2$ are the two principal values of the horizontal strain rate. For dislocation creep, we have the following:

$$\tau_s^{creep}(z) = \varphi \cdot exp\left(\frac{\beta + \xi z}{T}\right) \cdot \dot{e}_s$$

(Bird, 1989) where $\varphi = \frac{\alpha}{2}\left[2 \cdot \sqrt{-\dot{e}_1\dot{e}_2 - \dot{e}_1\dot{e}_z - \dot{e}_2\dot{e}_z}\right]^{\frac{1}{n-1}}$ with $\dot{e}_z = -(\dot{e}_1 + \dot{e}_2)$ and

$$\dot{e}_s = \begin{cases} \dfrac{\dot{e}_2 - \dot{e}_z}{2} & (\text{extension};\ \dot{e}_1 = 0) \\ \dfrac{\dot{e}_z - \dot{e}_1}{2} & (\text{compression};\ \dot{e}_2 = 0) \\ \sqrt{\dot{e}_1^2 + \dot{e}_2^2} \cdot \sin\left(tan^{-1}\dfrac{\dot{e}_2}{|\dot{e}_1|}\right) & (\text{transtension};\ |\dot{e}_1| < \dot{e}_2) \\ \sqrt{\dot{e}_1^2 + \dot{e}_2^2} \cdot \sin\left(\frac{\pi}{2} - tan^{-1}\dfrac{\dot{e}_2}{|\dot{e}_1|}\right) & (\text{transpression};\ |\dot{e}_1| > \dot{e}_2) \end{cases}$$

where α, β, ξ, and n are material constants, T is the temperature, $\dot{e}_s$ is the shear strain rate, and the tectonic regime depends on the ratio $\frac{\dot{e}_2}{\dot{e}_1}$. As for the shear stress $\dot{e}_S$, we emphasize that, in both the thrusting regime and the normal faulting regime, the location of the brittle/ductile transition is clear: it is the greatest depth of frictional behavior on any fault, which is also the greatest depth of frictional behavior on the most active fault set. However, in the strike-slip regime, the transition is less clear.

Applying the rule that the transition is found at the greatest depth of frictional behavior on any fault would create two discontinuities: one at the $\dot{e}_1 = 0$ axis, where normal faulting appears/disappears, and one at the $\dot{e}_2 = 0$ axis, where strike-slip faulting appears/disappears. Furthermore, the transition depth near these lines (on the deeper side) would be defined by the less active fault set, which becomes totally inactive as the line is approached. Choosing the alternate rule of taking the deepest frictional behavior on the most active fault set still results in two discontinuities, although at different places, with both in the strike-slip quadrant ($\dot{e}_1 < 0$, $\dot{e}_2 > 0$). To avoid these discontinuities, we followed the method of Bird (1999) and applied a sinusoidal smoothing to both the frictional and creep laws before computing the transition depth from the combination of values. This approach allows smoothing of the transition depth across each of the transpressional and transtensional wedges and satisfies the continuity conditions at $\dot{e}_1 = 0$, $\dot{e}_1 = -\dot{e}_2$, and $\dot{e}_1 = 0$.

The temperature T as a function of depth z is assumed to be in a conductive steady state given by the following (Bird, 1989):

$$T(z) = \begin{cases} T_s + \dfrac{q \cdot z}{k_c} - \dfrac{H \cdot z^2}{2k_c} & , z \leq z_c \\ T_c + \dfrac{(q - Hz_c) \cdot (z - z_c)}{k_m} & , z_c < z \end{cases}$$

where q is the surface heat-flow density, k_c and k_m are the conductivities of the crust and mantle, respectively (k in Table 2), z_c is the thickness of the crust, T_s and T_c are the temperatures at the surface and at the base of the crust, respectively, and H is the radiogenic heat-production rate within the crust (zero in the mantle).

For plastic deformation, we set the shear stress limit to τ_s^{plast}=500 MPa. This value, based on the plasticity limit of olivine (Griggs et al., 1960), has been shown to represent the deformation mechanisms in the mantle (Zang et al., 2007). Thus, we set τ_s(z)=min($\tau_s^{fric}, \tau_s^{creep}, \tau_s^{plast}$) where τ_s depends on the strain rate, temperature, and rheological parameters. The strength and shear stresses are studied in the continuum rather than along the modeled faults, and they thus represent the average behaviors of the three studied areas.

3.4. Model predictions and assumptions

The SHELLS program adopts the thin-shell approximation, i.e., it uses the vertical integration of lithospheric strength over triangular shell elements to reduce three-dimensional problems to two dimensions. With this approximation, the resulting horizontal velocity vectors are independent of depth. Model predictions include horizontal velocities and anelastic strain rates, which can be tested by comparison with GPS and stress data under some assumptions.

The shear stress is integrated along the *z* axis by means of one-km steps at each of the seven Gaussian integration points in each finite element (continuum or fault). The problem is reduced to two dimensions, and the corresponding strain solution is computed using only the in-plane terms. The vertical normal stress, assumed to be lithostatic, is then added to the result. Thus, bending stresses such as those occurring in the outer rises of subduction zones are not represented. Because vertical shear tractions on vertical planes are neglected, this approach can be successfully applied when the stress pattern is not affected by short-wavelength lateral changes in strength or density.

Over long time periods, velocity discontinuities exist across faults; these discontinuities are not observed in most short-term geodetic measurements. Over short time periods, temporary fault locking causes “interseismic” elastic strain. To quantitatively compare the horizontal anelastic velocities with the interseismic velocities obtained from GPS, we performed a correction for changes in the elastic strain rates that occur because of temporary fault locking (Savage, 1983; Liu and Bird, 2002). To constrain the stress regimes and stress directions under Andersonian conditions, we used data taken from the World Stress Map, which includes earthquake data. However, the *P* axis of individual earthquakes and the σ_1 stress orientations may diverge (McKenzie, 1969; Townend, 2006; Arnold and Townend, 2007). Assuming the continuum elements to be isotropic, the predicted principal stress axes have the same directions as the principal axes of the surface strain rates. Often, the maximum compressive horizontal stress (S_{Hmax}) shows good agreement with the directions of greatest compressive strain rate derived from GPS (Viganò et al., 2008; Keiding et al., 2009) although stress and strain rates can sometimes represent processes occurring on different timescales (Townend and Zoback, 2006).

The predicted stress regime (actually the strain-rate regime) is determined by the orientations of the principal strain-rate axes within the elements and off the modeled faults. The modeled S_{Hmax} direction was computed using the arctangents of the strain-rate eigenvalues $\dot{e}_1$ and $\dot{e}_2$. The regime was based on the relative stress magnitudes under the incompressible-flow assumption in a crust with no pre-existing faults where the vertical strain rates $\dot{e}_z = -(\dot{e}_1 + \dot{e}_2)$ were inferred from the horizontal rates. Close to the faults, anelasticity and fault slip affect the results and must be taken into account when the top of the fault is shallow with respect to the depth of the breakouts. In this work, the above assumptions satisfy the actual conditions fairly well; in fact, only a small percentage of the stress data in the three study areas is derived from a single focal mechanism in the IT and ET (Table 1), whereas in EX the stress ellipsoid cannot be recovered for only three data sets out of 76. Moreover, most of the faults are blind (Meletti et al., 2008) and are significantly deeper than the borehole data. Only two sets of borehole data were taken at depths below 4 km in the IT and ET. For the EX, the situation appears to be different because most of the data are derived from single-earthquake mechanisms and the active faults are relatively shallow. However, it appears that the model stress pattern is sufficiently smooth and that the S_{Hmax} directions inferred from earthquakes are mostly oriented NW–SE, i.e., parallel to the main trend of the fault, with reduced scatter (Figure 1). This observation was previously made by Barba and Basili (2000) for well-studied earthquakes in the area and suggests that the assumptions are also fairly well justified for the EX.

3.5. Model selection

The model goodness-of-fit for the simulation experiments was evaluated by the following tests:

- The horizontal velocities computed in a locked-fault state were compared with 182 interseismic GPS measurements in Italy (Devoti et al., 2010). The RMS of the residuals between the measured and computed velocities defines the GPS misfit, σ_{gps}.
- The directions of the principal stress axes, specifically, the directions of the principal axes of the anelastic strain rates, were compared with the directions of S_{Hmax} from the World Stress Map 2008 (Heidbach et al., 2008) located

within the model boundary. The average of the absolute angular differences between the measured and predicted directions (L1-norm) defines the S_{Hmax} misfit for Italy, σ_{stress}. The average absolute deviations between the measured and predicted directions within the three studied areas define the local S_{Hmax} misfits: ε_{EX}, ε_{IT}, and ε_{ET}.

- The model-predicted tectonic regimes (extension, compression, and strike-slip) in the continuum were compared with the focal mechanisms from the World Stress Map 2008 located within the study region. The percentage of predictions not matching the observed focal mechanisms defines the regime misfit for Italy, σ_{reg}.

We selected the most realistic simulations through a two-step comparison with the observed data. In the first step, we modeled the data over the whole region of Italy and discarded the simulations that showed any misfit (σ_{gps}, σ_{stress}, or σ_{reg}) greater than the 66^{th}-percentile value of the misfit distribution (Figure 3a). The remaining simulations were scored according to the corresponding local S_{Hmax} misfits (ε_{EX}, ε_{IT}, and ε_{ET}). The *N* best models for each region (EX, IT, and ET) were those exhibiting the lowest corresponding misfits (Figure 3b). In the second step, we computed the average shear stress $\tau_s(z)$, the strength $\Sigma = \int \tau_s(z)\, dz$, and the associated RMS for the *N* best simulations for each region. Thus, $\tau_s(z)$ and Σ were computed in each of the three study areas (Figures 4 and 5) and constitute our results.

3.6. Detailed IT crust model and tectonics

Assuming only one crustal layer in IT, the rheological parameters fall in between the EX and ET solutions (Table 3), as expected. However, the IT area is the transition zone across the margin between the Adriatic and the Tyrrhenian crust; the IT shows more complexity than the EX and the ET and cannot be represented satisfactorily by one crustal layer. In fact, two sedimentary layers are included in the crust of the flexured Adriatic lithosphere (Doglioni et al., 2007), which exhibits a differential behavior at depth (Negredo et al., 1999). Moreover, in the case of compressive tectonics the critical shear stress for brittle frictional sliding within the lower sedimentary layer can be close to the critical value for plastic deformation. Thus, we take a step forward and represent the upper crustal layer with the rheological parameters R1, a weak behavior corresponding to the overriding Tyrrhenian plate, and the lower sedimentary layer with R4, which has a high strength and corresponds to the subducting Adriatic plate. Here, we do not differentiate the mantle. Following such an approach in the IT area adds some freedom that we can minimize by assuming the same rheological parameters as in the adjacent areas and constraining all the remaining quantities in the numerical model. Here, we compute the average strength from the N best models $\Sigma = \langle\Sigma_i\rangle$. Then, similarly to Zoback and Townend (2001), we accommodate variations in the shear stress $\tau_s(z)$ by satisfying the strength constraint $\Sigma = \int \tau_s(z)\, dz$ where the strength, the heat flow q_{IT}, and the strain-rate eigenvalues ($\dot{e}_1$ and $\dot{e}_2$) are derived from the numerical model.

We calculated the shear stress $\tau_s(z)$ for compressive and transpressive tectonic behaviors as follows. On average, the base of the upper crust is at a depth of 18 km. To determine $\tau_s(z)$, we used the average heat flow (q_{IT} = 53 ± 5 mW/m^2) and strain-rate modulus ($\dot{e} = \sqrt{\dot{e}_1^2 + \dot{e}_2^2} = (8 \pm 2) \times 10^{-16}\ s^{-1}$) of the *N* best models for the IT. Within the *N* best models, the IT area showed compressional and transpressional tectonics that correspond to a horizontal strain-rate ratio with a wide range ($\dot{e}_2/\dot{e}_1 = 0 - 0.7$). To represent the tectonic behavior, we chose the extreme ends from this range of modeled ratios and determined that $\tau_s(z)$ for $\dot{e}_2/\dot{e}_1 = 0.7$ corresponds to transpressive tectonics, whereas it is 0 for the case of pure compression.

In the ET and EX, one layer within the crust is satisfactory, whereas in the IT the solution with two sedimentary layers is satisfactory only for depths shallower than 30 km. Understanding earthquakes deeper than 30 km in the IT (see Figure 5) would thus require a study using a different approach, which is outside the scope of this work.

3.7. Model uncertainties

To define the uncertainty of the results (the computed strengths Σ), we constructed a frequency distribution of the free parameters for a number of simulations. Here, *N* was chosen rather arbitrarily with the goal of balancing the robustness and significance of the results. If very few simulations are selected, the results depend on the measurement errors, whereas a larger value of *N* helps to obtain more robust results. If too many simulations are selected, the results depend on the ranges of the input parameters. We found it adequate to average the quantities over the best *N* = 50 models. However, a larger value of N was shown to be equally valid because the heat-flow and rheological parameters, which were our independent variables, were stable up to N = 200. We determined the uncertainty of the shear stress $\tau_s(z)$ through an examination of the percentiles of its frequency distribution. For practical considerations, we here report the 5th, 25th, 75th, and 95th percentiles of the best 50 models (Figure 5). The uncertainties of the results include the variabilities in the heat-flow values, sets of rheological parameters, and magnitudes of the basal tractions for the three independent parameters.

4. Results

We varied the heat flow, the rheological parameters, and the basal shear tractions in the appropriate ranges (Table 2) while performing 2016 simulations. Moving from east to west, we found a progressively shallower brittle-to-ductile transition in the crust and a sharp variation in the strength; the upper-plate region showed a very weak mantle, with a "crème brulée"-like behavior (Figure 5), whereas the forearc showed higher strength (Figure 4), especially in the lithospheric mantle.

The values at which the 66% cumulative percentage curves occur (Figure 3) are σ_{gps}= 1.55 mm/yr, σ_{stress}= 33°, and σ_{reg}= 78%. In the first step, 1333 simulations were discarded. The remaining 683 simulations were scored according to their ε_{EX}, ε_{IT}, and ε_{ET} values. The shear stress τ_s and total strength Σ were computed for the three study areas. The integrated strength and the associated uncertainties (standard deviation and percentiles) are shown in Figure 4. Here, it is clear that the strengths in the three target areas assumed significantly different values, and this result depended very little on the choice of the number N. The model-predicted stress orientations and interseismic velocities corresponding to the best 50 models showed little deviation from the observed data (Figure 6) within most of the study area.

Figure 5 displays the average shear stress at depth and the associated uncertainties corresponding to the best 50 models for the three areas. The large difference in the strengths translates to different rheological behaviors. The EX area showed to be very weak, with the strength concentrated within the upper crust. The mantle below the EX area appeared to be ductile. The ET area exhibited the largest strength of the three areas; this strength concentrated in the crust, which has a brittle rheology, and especially in the upper mantle, which behaves plastically. The IT area was somewhat transitional. The upper mantle exhibited the same plastic behavior as the ET, although with a reduced strength. The crust showed a more complicated behavior. The shallow sedimentary layer was predicted to be brittle. For the deeper sedimentary layer, the rheology depends on the parallelism between the transport direction of the thrust and the local stress direction; for pure compression, the rheology was plastic whereas for significant along-strike motion the rheology was predicted to be brittle.

For the ET area, the best 50 simulations according to their ε_{ET} values indicated a strength of Σ= 21 ± 6 TN/m within the compressive regime. In the crust, the peak shear stress was τ_s = 406 ± 94 MPa at a depth of 16–19 km. The shear-stress profile evidenced the plastic behavior of the upper mantle with a thickness of 25 km. The average deviations for the best 50 simulations were ε_{ET} = 38°, σ_{gps} = 1.48 mm/yr, σ_{stress} =3 3°, and σ_{reg} = 43%. The very high stress error ε_{ET} is likely the result of crustal heterogeneities not incorporated into the model. Thus, stress directions in ET were not always well predicted (Figure 6), but this issue had only a small effect on the resulting strength. The resulting heat-flow density was q_{ET} = 45 ± 4 mW/m^2, the strain rate ranged from 10^{-17}–10^{-15} s^{-1}, and the set of rheological parameters corresponded to average-to-high strength (Table 3 and Figure 5). For the IT area, the strength according to the ε_{IT} was Σ= 9 ± 4 TN/m and the tectonic regime was transpressive. In the crust, we found that τ_s = 188 MPa for transpressive mechanisms (τ_s = 327 MPa for reverse mechanisms) at a depth of 10 km for the upper sedimentary layer and τ_s = 380 MPa for transpressive mechanisms within the lower sedimentary layer (Figure 5). Here, the rheological behavior appears to be more complex because brittle frictional sliding was predicted for transpressive mechanisms in a 4-km thick layer, whereas in pure compression the lower sedimentary layer reached the plastic limit. Figure 7 illustrates the behavior of a thrust fault under the conditions determined for the IT area. The shear-stress profile for the upper mantle indicates that plastic behavior occurred within a thickness of 10 km. The average deviations were ε_{IT} = 23°, σ_{gps} = 1.50 mm/yr, σ_{stress} = 31°, and σ_{reg} = 58%. The tectonic-regime misfit here seems high; however, it was computed based on very few data (see Table 1), which makes the comparison with the regime nonsignificant. In contrast, the stress directions were well predicted (Figure 6). The heat-flow density was q_{IT} = 53 ± 5

mW/m^2, the strain rate ranged from 10^{-17}–10^{-15} s^{-1}, and the strength was high. The EX area showed an extensional regime; according to the ε_{EX}, the strength was $\Sigma = 0.6 \pm 0.2$ TN/m. In the crust, the peak τ_s was $\tau_s = 64 \pm 7$ MPa and was localized at a depth of 9–11 km. The upper mantle exhibited ductile behavior, with a peak of $\tau_s = 30 \pm 20$ MPa (Figure 5). The average deviations for the 50 best simulations were $\varepsilon_{EX} = 14°$, $\sigma_{gps} = 1.54$ mm/yr, $\sigma_{stress} = 33°$, and $\sigma_{reg} = 32\%$. We found a heat-flow density of $q_{EX} = 66 \pm 4$ mW/m^2, a strain rate of 10^{-17}–10^{-15} s^{-1}, and a very weak lithosphere (Table 3). The heat-flow values that we determined within the three areas (q_{EX}, q_{IT}, and q_{ET}) are consistent with the values reported in the literature (Pasquale et al., 1997; Della Vedova et al., 2001). To understand the entirety of the model's limitations, we also compared, in the three areas, the average topographic elevations computed assuming local isostasy with the average actual topography used in the numerical model. We found that the differences were less than 200 m, with a positive residual in EX and a negative residual in ET (see the horizontal dashed lines in Figure 5). These differences, which are less than those obtained by Carminati et al. (2001) along a very similar profile, depend on the model assumptions, as the plate flexure was not modeled. We consider these differences to be acceptable and consistent with the model's limitations.

5. Discussion

The strength of the lithosphere can vary drastically within a few kilometers across a subduction margin, changing from a strong upper mantle in the continental lithosphere to a weak crust and ductile upper mantle in the accretionary prism. A trial-and-error approach was used to determine the basic parameters to calculate Σ—i.e., the rheological parameters and heat flow—and to find the values that minimized the differences between the measured data and the predicted quantities. The uncertainties associated with the heat flow and the strength were relatively low, which suggests that it is possible to determine the heat flow and the average rheological behavior when sufficient surface data related to the deformation are available. The approach used in this paper does not require extrapolation of laboratory rheologies from cm-sized samples to a large-scale scenario.

Our results proved to be stable within the stated uncertainties. However, a lower value of the plasticity limit for the upper crustal sediments, e.g., τ_s^{plast} = 250 MPa, can reduce the thickness of the brittle layer. The uncertainties in the shear stress and the strength because of crustal thickness and strain rate are negligible, but they affect the depth at which the peak shear stress occurs. The shear-stress profile also depends on the choice of rheological stratification within the crust. Although our method performs well at reconstructing the total strength, the average rheological behavior, and the heat flow, the model requires knowledge about the thicknesses of the sedimentary layers within the crust to reconstruct the details of shear-stress profiles.

The results of our model agree with those of Dragoni et al. (1996) in that the crust accounts for nearly all of the lithospheric strength of the EX because the mantle exerts a negligible resistance to deformation. A clue to the existence of an aseismic mantle also comes from Chiarabba et al. (2009), who, by means of tomographic studies, observed low P-wave velocities within the upper mantle. Our results confirm that the upper mantle below the extensional area is aseismic.

The ET area, which is part of the Adriatic domain, exhibited the highest strength. High values of Σ depend on a stronger rheology and a lower heat-flow density. Such high strength favors the accumulation of deformations on pre-existing structures or along weaker detachment layers within or at the border of the Adriatic microplate (Lavecchia et al., 1994; Ivancic et al., 2006; Scisciani and Calamita, 2009). The increase in lithospheric strength when moving eastward from this area toward the Adriatic Sea has been well documented (Dragoni et al., 1996; Tesauro et al., 2009; Pauselli et al., 2010). Our results, which were obtained by minimizing misfits with respect to GPS measurements, S_{Hmax}, and focal-mechanism solutions, confirm a difference of approximately 1–1.5 orders of magnitude between the strength Σ of the EX and those of the IT and ET.

The IT showed greater rheological complexity than the other two areas. To account for the change in tectonic stress at depth and/or the vertical separation in the seismicity, two crustal sedimentary layers are required in the IT model, with a discontinuity at a depth of 18 km. Because of the limitations of the thin-shell approach, changes of the tectonic regime with the depth (e.g., extension at the surface or compression at depth) cannot be reproduced. Conversely, the stress axes were well reproduced, and we focused on the behavior at depth within the compressive volume. When two sedimentary layers are modeled, the shear-stress profile for the deeper layer strongly depends on the angle between $\dot{e}_1$ and $\dot{e}_2$. Plastic deformation occurs for nearly pure compression. However, frictional sliding takes place for transpressive and strike-slip mechanisms, which makes the lateral ramps, i.e., the portion of the thrust with some or significant along-strike movement of the compressed material, the least resistant and the most prone to earthquakes. Figure 7 illustrates the behavior of a thrust fault under the conditions determined for the IT area. The brittle frictional sliding predicted by the shear stress model at a ~20-km depth (Figure 5) in the case of transpression is represented by the lateral ramps (labeled "B" at a ~20-km depth in Figure 7), whereas the plastic behavior predicted in pure compression is illustrated by the frontal ramp (labeled "P" in Figure 7). The brittle and plastic behaviors coexist to varying degrees depending on the parallelism of the transport direction with the local S_{Hmax} direction. This coexistence can be generalized to areas with characteristics similar to IT. It could be worth exploring the range of heat flows and rheological parameters where a plastic-to-fragile transition is predicted to occur along the strike of the thrust.

These results suggest that oblique thrusts and the formation of lateral ramps are favored during the evolution of a thrust system because they require less energy. If we assume that the total energy involved in the process is constant, we can expect that the formation of lateral ramps allows the thrust system to focus the energy on the frontal ramp where along-dip movement occurs; in this way, it plays a major role in the evolution of a thrust system at depth. Moreover, the coexistence of brittle and plastic behaviors along the deeper portion of the thrust indicates that the seismogenic behavior of the area depends on the angle between the thrust strike and the regional compressive stress direction. This observation could benefit seismic-hazard studies.

Field data (Vannoli et al., 2004), seismicity (Frepoli and Amato, 1997), and borehole breakouts (Montone et al., 2004) all address compression and extension, but they do not provide any information about strength. This work is the first to use all of the available surface geophysical data to quantify the strength of this area; furthermore, the strength was determined without extrapolating laboratory rheologies from centimeter-sized samples to a large scale. Our approach allows us to identify sharp transitions between strong and weak behaviors when information at depth is scarce and to complement laboratory and field work with respect to time, horizontal distance, and depth.

Acknowledgements

We thank Peter Bird for discussions and for making his code SHELLS available. Three anonymous reviewers greatly helped in improving the manuscript. Michele M.C. Carafa was supported by a grant from DPC-INGV project S1 (2008-2010).

References

Arnold, R., and J. Townend (2007), A Bayesian approach to estimating tectonic stress from seismological data, *Geophys. J. Int.*, *170*(3), 1336-1356.

Babuska, V., and J. Plomerova (2006), European mantle lithosphere assembled from rigid microplates with inherited seismic anisotropy, *Phys. Earth Planet. Int.*, *158*, 264–280, doi:10.1016/j.pepi.2006.01.010.

Barba S. and R. Basili (2000), Analysis of seismological and geological observations for moderate-size earthquakes: the Colfiorito Fault System (Central Apennines, Italy), *Geophys. J. Int.*, *141*, 241–252.

Barba, S., M.M.C. Carafa, and E. Boschi E. (2008), Experimental evidence for mantle drag in the Mediterranean, *Geophys. Res. Lett.*, 35, L06302, doi:10.1029/2008GL033281.

Barba, S., M.M.C. Carafa, M.T. Mariucci, P. Montone, and S. Pierdominici S. (2010), Present-day stress-field modelling of southern Italy constrained by stress and GPS data, *Tectonophysics*, in press, doi:10.1016/j.tecto.2009.10.017.

Basili, R., and S. Barba (2007), Migration and shortening rates in the northern Apennines, Italy: implications for seismic hazard, *Terra Nova*, *19*(6), 462–468, doi: 10.1111/j.1365-3121.2007.00772.x.

Basili, R., G. Valensise, P. Vannoli, P. Burrato, U. Fracassi, S. Mariano, M. Tiberti, and E. Boschi (2008), The database of individual seismogenic sources (DISS), version 3: Summarizing 20 years of research on Italy’s earthquake geology, *Tectonophysics*, *453*(1-4), 20–43.

Becker, T. W., Hardebeck, J. L., and G. Anderson (2005) Constraints on fault slip rates of the southern California plate boundary from GPS velocity and stress inversions. *Geophys J. Int.*, *160*, 634-650.

Bird, P. (1989), New finite element techniques for modeling deformation histories of continents with stratified temperature-dependent rheologies, *J. Geophys. Res.*, *94*(B4), 3967-3990.

Bird, P. (1999), Thin-plate and thin-shell finite-element programs for forward dynamic modeling of plate deformation and faulting. Comp. Geosci., 383–394.

Bird, P., Z. Ben-Avraham, G. Schubert, M. Andreoli, and G. Viola (2006), Patterns of stress and strain rate in southern Africa, *J. Geophys. Res.*, *111*, B08402, doi:10.1029/2005JB003882.

Bodine, J. H., M. S. Steckler, and A. B. Watts (1981), Observations of flexure and the rheology of the oceanic lithosphere, *J. Geophys. Res.*, *86*(B5), 3695-3707.

Boncio, P., and G. Lavecchia (2000), A structural model for active extension in Central Italy, *J. Geodyn.*, *29*, 233-244.

Boncio, P., G. Lavecchia, and B. Pace (2004), Defining a model of 3D seismogenic sources for seismic hazard assessment applications: the case of Central Apennines (Italy), *J. Seismol.*, *8*, 407-425.

Brace, W. F., and D. L. Kohlstedt (1980), Limits on lithospheric stresses imposed by laboratory experiments, *J. Geophys. Res.*, *85*(B11), 6248–6252.

Burgmann, R., and G. Dresen (2008), Rheology of the lower crust and upper mantle: Evidence from rock mechanics, geodesy and field observations, *Ann. Rev. Earth Plan. Sci.*, *36*, 531-567, doi:10.1146/annurev.earth.36.031207.124326.

Burov, E. B. and A. B. Watts (2006), The long-term strength of continental lithosphere: "jelly sandwich" or "crème-brûlé"?, *GSA Today*, *16*, 4-10.

Calcagnile, G., and G. F. Panza (1980), The main characteristics of the lithosphere-asthenosphere system in Italy and surrounding regions, *Pure Appl. Geophys.*, *119*(4), 865–879.

Caporali, A. (2009), Present day horizontal velocities of permanent GPS stations and the implied regional strain rate field, 1st annual meeting of Seismological Projects, 19-21 October 2009, Rome, http://portale.ingv.it/l-ingv/progetti/progetti-finanziati-dal-dipartimento-di-protezione-civile-1/progetti-dpc-convenzione-2007-2009/progetti-s/first-annual-meeting/

Carminati E., F. Toniolo Augier and S. Barba (2001), Dynamic modelling of stress accumulation in central Italy: Role of structural heterogeneities and of rheology, *Geophys. J. Int.*, *144*, 373-390.

Chiarabba, C., P. De Gori, and F. Speranza (2009), Deep geometry and rheology of an orogenic wedge developing above a continental subduction zone: Seismological evidence from the northern-central Apennines (Italy), *Lithosphere, 1*, 95-104.

D'Agostino, N., S. Mantenuto, E. D'Anastasio, A. Avallone, M. Barchi, C. Collettini, F. Radicioni, A. Stoppini, and G. Fastellini (2008), Contemporary crustal extension in the Umbria-Marche Apennines from regional CGPS networks and comparison between geodetic and seismic deformation, *Tectonophysics*, *476*(1-2), 3-12.

Della Vedova, B., S. Bellani, G. Pellis, and P. Squarci (2001), Deep temperatures and surface heat flow distribution. In: Anatomy of an orogen, The Apennines and adjacent Mediterranean basins, Vai G.B., Martini I.P. editori, Kluwer Academy Publishers, Dordrecht, The Netherlands, 65-76.

Devoti, R., F. Riguzzi, M. Cuffaro, and C. Doglioni (2008), New GPS constraints on the kinematics of the Apennines subduction, *Earth Planet. Sci. Lett.*, *273*, 163–174.

Devoti R., G. Pietrantonio, A. Pisani, F. Riguzzi and E. Serpelloni, (2010) Present day kinematics of Italy, In: (Eds.) Marco Beltrando, Angelo Peccerillo, Massimo Mattei, Sandro Conticelli, and Carlo Doglioni, The Geology of Italy, *Journal of the Virtual Explorer*, Electronic Edition, ISSN 1441-8142, volume 36, paper 2.

DISS Working Group (2006), Database of Individual Seismogenic Sources (DISS), Version 3.0.2: A compilation of potential sources for earthquakes larger than M 5.5 in Italy and surrounding areas, http://www.ingv.it/DISS/. Available at http://hdl.handle.net/2122/2412.

Doglioni, C., S. Barba, E. Carminati, and F. Riguzzi (2010), Role of the brittle-ductile transition on fault activation, Phys. Earth Planet. Int., doi:10.1016/j.pepi.2010.11.005

Doglioni, C., E. Gueguen, P. Harabaglia, and F. Mongelli (1999), On the origin of W-directed subduction zones and applications to the western Mediterranean, In: Durand, B., Jolivet, L., Horvath, F., and Séranne, M. (eds.), The Mediterranean basins, Tertiary extension within the Alpine orogen, *Geol. Soc. Lon. Sp. Publ.*, *156*, 541-561.

Doglioni, C., F. Mongelli, and G. P. Pialli (1998), Boudinage of the Alpine belt in the Apenninic back-arc, *Mem. Soc. Geol. It.*, *52*, 457-468.

Doglioni, C., E. Carminati, M. Cuffaro, and D. Scrocca D. (2007), Subduction kinematics and dynamic constraints, *Earth Sci. Rev.*, *83*, 125-175, doi:10.1016/j.earscirev.2007.04.001.

Dragoni, M., C. Doglioni, F. Mongelli, and G. Zito (1996), Evaluation of stresses in two geodynamically different areas: stable foreland and extensional backarc, *Pure Appl. Geophys.*, *146*(2), 319-341.

Evans, B. (2005), Creep constitutive laws for rocks with evolving structure, *Geol. Soc. Lon. Sp. Publ.*, *245*, 329–346.

Flesch L. F., W. E. Holt, A. J. Haines and B. Shen-Tu (2000), Dynamics of the Pacific-North American Plate Boundary in the Western United States, *Science, 287,* 834-836.

Frepoli, A., and A. Amato (1997), Contemporaneous extension and compression in the Northern Apennines from earthquake fault-plane solutions, *Geophys. J. Int.*, *129*, 368–388.

Griggs, D.T., F.J. Turner, and H.C. Heard (1960), Deformation of rocks at 500° to 800°C. In: Griggs, D.T., Handin, J. (Eds.), Rock Deformation. *Geol. Soc. Am. Mem.*, *79*, 39–104.

Handy, M. R., and J. P. Brun (2004), Seismicity, structure and strength of the continental lithosphere, *Earth Planet. Sci. Lett.*, *223*(3-4), 427-441.

Heidbach, O., M. Tingay, A. Barth, J. Reinecker, D. Kurfeß, and B. Müller (2008), The World Stress Map database release 2008, doi:10.1594/GFZ.WSM.Rel2008

Hirth, G, and D.L. Kohlstedt (2003), Rheology of the upper mantle and the mantle wedge: a view from the experimentalists. In: Eiler J. (Ed.), Inside the Subduction Factory, 83–105, Geophys. Monograph 138, Am. Geophys. Soc. Washington, DC.

Ivančić, I., D. Herak, S. Markušić, I. Sović, and M. Herak (2006), Seismicity of Croatia in the period 2002–2005, *Geofizika*, *23*(2), 87–103.

Jackson, J. (2002), Strength of the continental lithosphere: Time to abandon the jelly sandwich? *GSA Today*, *12*(9), 4–10.

Karato, S. (2008), Deformation of Earth Materials: An Introduction to the Rheology of Solid Earth, Cambridge University Press.

Keiding M., B. Lund, and T. Árnadóttir (2009), Earthquakes, stress, and strain along an obliquely divergent plate boundary: Reykjanes Peninsula, southwest Iceland, *J Geophys. Res.*, *114*, B09306, doi:10.1029/2008JB006253.

Kong X. and P. Bird (1995), SHELLS: A thin-shell program for modeling neotectonics of regional or global lithosphere with faults, *J. Geophys. Res.*, *100*(Bll), 22,129-22,131.

Lamontagne M. and G. Ranalli (1996), Thermal and rheological constraints on the earthquake depth distribution in the Charlevoix, Canada, intraplate seismic zone, *Tectonophysics*, *257*(1), 55-69.

Lavecchia G., F. Brozzetti, M. Barchi M., J. Keller, and M. Menichetti (1994), Seismotectonic zoning in east- central Italy deduced from an analysis of the Neogene to Present deformations and related stress fields, *Bull. Soc. Geol. Am.*, *106*, 1107-1120.

Marone F., M. van der Meijde, S. van der Lee, D. Giardini (2003), Joint inversion of local, regional and teleseismic data for crustal thickness in the Eurasia-Africa plate boundary region, *Geophys. J. Int.*, *154*, 499–514.

McKenzie D.P. (1969), The relation between fault plane solutions for earthquakes and the directions of the principal stress, *Bull. Seismol. Soc. Am.*, *59*, 591–601.

Meletti C., F. Galadini, G. Valensise, M. Stucchi, R. Basili, S. Barba, G. Vannucci, E. Boschi (2008). The ZS9 seismic source model for the seismic hazard assessment of the Italian territory. *Tectonophysics*, *450* (1), 85–108. doi:10.1016/j.tecto.2008.01.003.

Michetti, A. M., F. Brunamonte, L. Serva, and E. Vittori (1996), Trench investigations of the 1915 Fucino earthquake fault scarps (Abruzzo, central Italy): geological evidence of large historical events, *J. Geophys. Res.*, *101*(B3), 5921–5936.

Montone, P., M.T. Mariucci, S. Pondrelli, and A. Amato (2004), An improved stress map for Italy and surrounding regions (central Mediterranean), *J. Geophys. Res.*, *109*(B10), 10410.

Negredo, A.M., E. Carminati, S. Barba, R. Sabadini, (1999), Dynamic modelling of stress accumulation in central Italy, *Geophys. Res. Lett.*, *26*, 1945–1948.

Nicolich, R. (2001), Deep Seismic Transects. In: G. B. Vai and P. Martini (Eds.), Anatomy of an orogen: the Appennines and Adjacent Mediterranean Basins, Kluver Acad. Publishers, 47-52.

Rey, P., O. Vanderhaeghe, and C. Teyssier (2001), Gravitational collapse of the continental crust: definition, regimes and modes, *Tectonophysics*, *342* (3-4), 435-449.

Papanikolaou, I.D., and Roberts G.P. (2007), Geometry, kinematics and deformation rates along the active normal fault system in the Southern Apennines: implications for fault growth, *J. Struct. Geol.*, *29*, 166-188.

Pasquale, V., M. Verdoya, and P. Chiozzi (1999), Thermal state and deep earthquakes in the Southern Tyrrhenian, *Tectonophysics*, *306*, 435–448.

Pasquale, V., M. Verdoya, P. Chiozzi, and G. Ranalli (1997), Rheology and seismotectonic regime in the northern central Mediterranean, *Tectonophysics*, *270*, 239-257.

Pauselli, C., and C. Federico (2002), The brittle/ductile transition along the Crop03 seismic profile: relationship with the geological features, *Boll. Soc. Geol. It.*, *121*, 25-35.

Pauselli C., G. Ranalli, and C. Federico (2010), Rheology of the Northern Apennines: Lateral variations of lithospheric strength, *Tectonophysics*, in press, doi:10.1016/j.tecto.2009.08.029

Pialli, G., M. R. Barchi, and G. Minelli (Eds.) (1998), Results of the CROP 03 deep seismic reflection profile, *Mem. Soc. Geol. Ital.*, *52*, 657 pp.

Pollitz, FF, G. Peltzer, and R. Burgmann (2000), Mobility of continental mantle: evidence from postseismic geodetic observations following the 1992 Landers earthquake, *J. Geophys. Res.*, *105*(B4), 8035–8054.

Pondrelli, S., Salimbeni, S., Ekstrom, G., Morelli, A., Gasperini, P., Vannucci, G. (2006), The Italian CMT dataset from1977 to the present, *Phys. Earth Planet. Inter.*, *159*, 286–303.

Savage J. C. (1983), A dislocation model of strain accumulation and release at a subduction zone, *J. Geophys. Res.*, *88*, 4984– 4996.

Scisciani, V., and F. Calamita (2009), Active intraplate deformation within Adria: Examples from the Adriatic region, *Tectonophysics*, *476*(1-2), 57-72.

Scrocca, D., M. Livani, S. Bigi, and E. Carminati (2009), Seismotectonic charaterization of the central-northern Apennines accretionary prism, 1st annual meeting of Seismological Projects, 19-21 October 2009, Rome, http://portale.ingv.it/l-ingv/progetti/progetti-finanziati-dal-dipartimento-di-protezione-civile-1/progetti-dpc-convenzione-2007-2009/progetti-s/first-annual-meeting/

Scrocca, D., E. Carminati, C. Doglioni, and D. Marcantoni (2007), Slab retreat and active shortening along the central-northern Apennines. In: Thrust belts and Foreland Basins: From Fold Kinematics to Hydrocarbon Systems, O. Lacombe, J. Lavé, F. Roure and J. Verges (Eds.), Frontiers in Earth Sciences, Springer, 471-487.

Serpelloni, E., G. Vannucci, S. Pondrelli, A. Argnani, G. Casula, M. Anzidei, P. Baldi, and P. Gasperini (2007), Kinematics of the Western Africa–Eurasia plate boundary from focal mechanisms and GPS data, *Geophys. J. Int.*, *169*(3), 1180–1200.

Sibson, R.H., S.H. White, and B.K. Atkinson (1979), Fault rock distribution and structure within the Alpine Fault Zone: a preliminary account, *Bull. R. Soc. N.Z.*, *18*, 55–65.

Thatcher, W. (1983), Nonlinear strain buildup and the earthquake cycle on the San Andreas fault, *J. Geophys. Res.*, *88*(B7), 5893–5902.

Thatcher W. (2009), How the continents deform: the evidence from tectonic geodesy, *Ann. Rev. Earth Plan. Sci.*, *37*, 14.1–14.26.

Townend J. (2006), What do faults feel? Observational constraints on the stresses acting on seismogenic faults, In Earthquakes: Radiated Energy and the Physics of Faulting, edited by R. Abercrombie, A. McGarr, H. Kanamori, and G. Di Toro, American Geophysical Union Geophysical Monograph Series, *170*, 313–327.

Townend, J., and M. D. Zoback (2006), Stress, strain, and mountain building in central Japan, *J. Geophys. Res.*, *111*, B03411, doi:10.1029/2005JB003759.

Tullis, J. (2002), Deformation of crustal materials, *Rev. Mineral.*, *51*, 51–95

Twiss, R. J. (1977), Theory and applicability of a recrystallized grain size paleopiezometer, *Pure Appl. Geophys.*, *115*, 227–44.

Vannoli P., R. Basili and G. Valensise (2004), New geomorphic evidence for anticlinal growth driven by blind-thrust faulting along the northern Marche coastal belt (central Italy), *J. Seismol., 8*, 297-312.

Verdoya M., V. Pasquale and P. Chiozzi (2005), Thermo-mechanical evolution and rheology of the northern sector of the Tyrrhenian–Apennines system, *J. Volcanol. Geotherm. Res.*, *148*(1–2), 20–30.Watts, A.B. (2001), Isostasy and Flexure of the Lithosphere, Cambridge University Press.

Viganò A. , Bressan G., Ranalli G. and S. Martina (2008),Focal mechanism inversion in the Giudicarie–Lessini seismotectonic region (Southern Alps, Italy): Insights on tectonic stress and strain, *Tectonophysics*, *460*(1-4), 106-115.

Zoback M.D. and J. Townend (2001), Implication of hydrostatic pore pressure and high crustal strength for the deformation of intraplate lithosphere, *Tectonophysics, 336*, 19-30.

Zang, S.X., R.Q. Wei, and J.Y. Ning (2007), Effect of the brittle fracture on the rheological structure of the lithosphere and its applications in the Ordos, *Tectonophysics*, *429,* 267-285.

Zhang, S., S-I. Karato (1995), Lattice preferred orientation of olivine aggregates deformed in simple shear, *Nature*, *375*, 774–77.

Zoback, M.D., J. Townend and B. Grollimund (2002), Steady-state failure equilibrium and deformation of intraplate lithosphere, *Int. Geol. Rev., 44*, 383-401.

Figure captions

Figure 1. Study area. The gray ribbons represent composite seismogenic sources (Basili et al., 2008), the black arrows indicate GPS-measured horizontal velocities (Devoti et al., 2010), and the gray bars represent S_{Hmax} orientations from WSM08 (Heidbach et al., 2008). The dashed line represents the section of Figure 5, and the light-gray triangles are finite elements. The inset shows the model edges, the boundary condition codes, the area of application of the basal tractions and their direction, and the model faults. The “beach balls” represent characteristic earthquakes for the three areas (EX, Normal fault, 26/9/1997, Mw = 5.7; IT, 21/10/2006, Mw = 4.3; ET, Thrust fault, 3/7/1987, Mw = 5.1; data from Pondrelli et al., 2006). EX: extensional tectonics along the Apennines; IT: internal thrust (deeper thrust, mixed kinematics); ET: external thrust.

Figure 2. Flow chart of the trial-and-error procedure. σ_{gps}, RMS of residuals between the measured GPS velocities and the model velocities in the locked-fault state; σ_{stress}, average angular difference between the measured and predicted S_{Hmax} directions; ε_{EX}, ε_{IT}, and ε_{ET}, as in σ_{stress} but with S_{Hmax} directions located in the specified area; σ_{reg}, percentage of predictions not matching the observed focal mechanisms.

Figure 3. (a) Cumulative percentage curves for GPS misfit, S_{Hmax} misfit, and bad regime. The thick black line shows the number of simulations passing the first-step selection as a function of the cumulative percentage. The vertical black line indicates the first selection level at 66%. (b) The S_{Hmax} misfit of the 200 best simulations according to ε_{EX}, ε_{IT}, and ε_{ET}.

Figure 4. Strength versus simulation number. Black (solid colored) line, strength average; solid gray (dashed colored) lines, 95% confidence limits; error bars, standard deviation.

Figure 5. Rheological profiles of the three studied areas. The trace A-A’ of this section is shown in Figure 1. Thick black lines, average rheological profiles for the

EX, IT, and ET; light gray (light green) bands, 5th–95th percentile intervals; dark gray (dark green) bands, 25th–75th percentile intervals. For the internal thrust (IT), the profiles for the transpressive regime (black line; lateral ramps labeled "B" at a ~20-km depth in Figure 7) and for pure compression (dotted line; frontal ramp labeled "P" in Figure 7) are shown. The labeled thin lines indicate the features included in the model and projected onto the section A-A': topography (T, 10X vertical scale; brown/blue colors indicate above and below the sea level); the base of the sedimentary layer (S); the depth of the Moho (M) with its error (grid); the base of the lithosphere (L); the Alto-Tiberina normal fault (NF); and the thrust faults (TF). The dashed lines S and M represent the subducting layers; S, M, NF, and TF are modified from Doglioni et al. (1998) with the exception of the starred Moho (M*), which was introduced in the construction of the mechanical model. The dashed horizontal lines within the topography panel represent the topographic elevations computed assuming local isostasy for the three areas; the predicted average elevation differs by less than 200 m from the observed average topography. The dots represent the earthquakes that occurred in the study area during the period 2005–2009. The scale for the shear stress (0–500 MPa) is the same for the three rheological profiles. Horizontal and vertical scales are the same with the exceptions of topography (10X).

Figure 6. Model outputs. (a) Modeled S_{Hmax} orientations and tectonic regimes compared with WSM08 data (Heidbach et al., 2008); (b) GPS velocities (black) with 1σ error (data from Devoti et al., 2010) and modeled interseismic velocities (gray arrows).

Figure 7. Sketch of the rheological behavior of the internal thrust. Gray, brittle frictional sliding; silver, dislocation creep; dark gray, plastic deformation. Along the lateral ramps at intermediate depth (~20 km), the model predicts brittle frictional sliding (B) whereas in the frontal ramp it predicts plastic behavior (P).

Table captions

Table 1. Summary of the data used to constrain the model. ALL, data within the model boundary; EX, IT, and ET, data within the three target areas. Data marked with (*) are listed for reference only and do not constitute an independent misfit measure.

Table 2. Model parameters.

Table 3. Frequency distribution of the 50 best experiments for each area as a function of heat-flow density and rheological parameters. The gray shading indicates more frequent combinations. R1–4 are as in Table 2.

Data type	Misfit name	Types of stress indicators	N. of data vs. Quality Ranking			
			A	B	C	D
S_{Hmax}	σ_{stress}	Earthquake focal mechanisms (*)	2	3	700	316
		Well bore breakouts (*)	36	98	104	114
		Hydraulic fractures (*)	8	5	3	4
		Overcoring data (*)	-	1	11	55
		Geologic fault-slip data (*)	-	1	14	-
		Others (*)	1	-	1	18
		All data (ALL)	**47**	**108**	**833**	**507**
	ε_{EX}	Earthquake focal mechanisms (*)	1	-	74	2
		Well bore breakouts (*)	-	-	1	1
		Geologic fault-slip data (*)	-	-	1	-
		All data (EX)	**1**	**-**	**76**	**3**
	ε_{IT}	Earthquake focal mechanisms (*)	-	-	3	2
		Well bore breakouts (*)	-	4	7	6
		Overcoring data (*)	-	-	-	1
		All data (IT)	**-**	**4**	**10**	**9**
	ε_{ET}	Earthquake focal mechanisms (*)	1	-	1	3
		Well bore breakouts (*)	1	6	10	21
		All data (ET)	**2**	**6**	**11**	**24**

Data type	Misfit name		N. of data vs. Deformation mechanism			
			NF	SS	TF	U
Tectonic regime	σ_{reg}	**All data (ALL)**	**391**	**377**	**316**	**411**

Data type	Misfit name		N. of data vs. area			
			ALL	EX	IT	ET
GPS	σ_{gps}	**All data (ALL)**	**182**	17(*)	5(*)	4(*)

Table 1. Summary of the data used to constrain the model. ALL, data within the model boundary; EX, IT, and ET, data within the three target areas. Data marked with (*) are listed for reference only and do not constitute an independent misfit measure.

Table 2. Model parameters.

<table>
<tr><th>Symbol</th><th colspan="2">Represents</th><th>Crust</th><th>Mantle</th><th>No. Steps</th></tr>
<tr><td>ρ_{litho}</td><td colspan="2">Mean density ($kg \cdot m^{-3}$)</td><td>2850</td><td>3300</td><td>1</td></tr>
<tr><td>k</td><td colspan="2">Thermal conductivity ($W \cdot m^{-1} \cdot K^{-1}$)</td><td>3.0</td><td>3.4</td><td>1</td></tr>
<tr><td>H</td><td colspan="2">Radioactive heat production ($W \cdot m^{-3}$)</td><td>8.0 10^{-7}</td><td>0</td><td>1</td></tr>
<tr><td>T_s</td><td colspan="2">Surface temperature (K)</td><td colspan="2">273</td><td>1</td></tr>
<tr><td>ρ_{H_2O}</td><td colspan="2">Mean density of water ($kg \cdot m^{-3}$)</td><td colspan="2">1030</td><td>1</td></tr>
<tr><td>q_{EX}</td><td colspan="2">Heat flow density in EX (mW/m^2)</td><td colspan="2">61-64-…-79</td><td>7</td></tr>
<tr><td>q_{IT}</td><td colspan="2">Heat flow density in IT (mW/m^2)</td><td colspan="2">40-43-…-61</td><td>8</td></tr>
<tr><td>q_{ET}</td><td colspan="2">Heat flow density in ET (mW/m^2)</td><td colspan="2">40-43-…-61</td><td>8</td></tr>
<tr><td>Φ</td><td colspan="2">Shear basal traction intensity (MPa)</td><td colspan="2">15-20-…-50</td><td>8</td></tr>
<tr><td>α</td><td colspan="2">Pre-exponential constant in creep rheology (MPa)</td><td>2.11</td><td>0.0128</td><td>1</td></tr>
<tr><td rowspan="4">β</td><td rowspan="4">Temperature coefficient in creep rheology (K^{-1})</td><td>R1</td><td>8625</td><td>18028</td><td rowspan="4">4</td></tr>
<tr><td>R2</td><td>9625</td><td>18528</td></tr>
<tr><td>R3</td><td>10650</td><td>19028</td></tr>
<tr><td>R4</td><td>11650</td><td>19528</td></tr>
<tr><td>ξ</td><td colspan="2">Depth coefficient in creep rheology ($K\ m^{-1}$)</td><td>0</td><td>0.0171</td><td>1</td></tr>
<tr><td>n</td><td colspan="2">Stress exponent in creep rheology</td><td colspan="2">2.4</td><td>1</td></tr>
<tr><td>τ_s^{plast}</td><td colspan="2">Critical shear stress in plastic rheology (MPa)</td><td colspan="2">500</td><td>1</td></tr>
<tr><td>μ</td><td colspan="2">Standard coefficient of friction</td><td colspan="2">0.85</td><td>1</td></tr>
<tr><td>λ</td><td colspan="2">efficacy of the pore pressure</td><td colspan="2">1</td><td>1</td></tr>
</table>

Table 3. Frequency distribution of the 50 best experiments for each area as a function of heat-flow density and rheological parameters. The gray shading indicates more frequent combinations. R1–4 are as in Table 2.

	Area	EX				IT				ET			
	Rheology	R1	R2	R3	R4	R1	R2	R3	R4	R1	R2	R3	R4
Heat flow (mW/m^2)	79	-	1	-	-	-	-	-	-	-	-	-	-
	76	-	1	-	-	-	-	-	-	-	-	-	-
	73	3	1	-	-	-	-	-	-	-	-	-	-
	70	7	-	-	-	-	-	-	-	-	-	-	-
	67	11	-	-	-	-	-	-	-	-	-	-	-
	64	13	-	-	-	-	-	-	-	-	-	-	-
	61	13	-	-	-	-	-	-	5	-	-	-	-
	58	-	-	-	-	-	-	-	7	-	-	-	-
	55	-	-	-	-	-	-	6	4	-	-	-	3
	52	-	-	-	-	-	2	10	3	-	-	-	2
	49	-	-	-	-	-	6	1	1	-	-	4	1
	46	-	-	-	-	-	3	-	-	-	-	7	5
	43	-	-	-	-	-	2	-	-	-	15	4	4
	40	-	-	-	-	-	-	-	-	-	5	-	-
Total		47	3	0	0	0	13	17	20	0	20	15	15

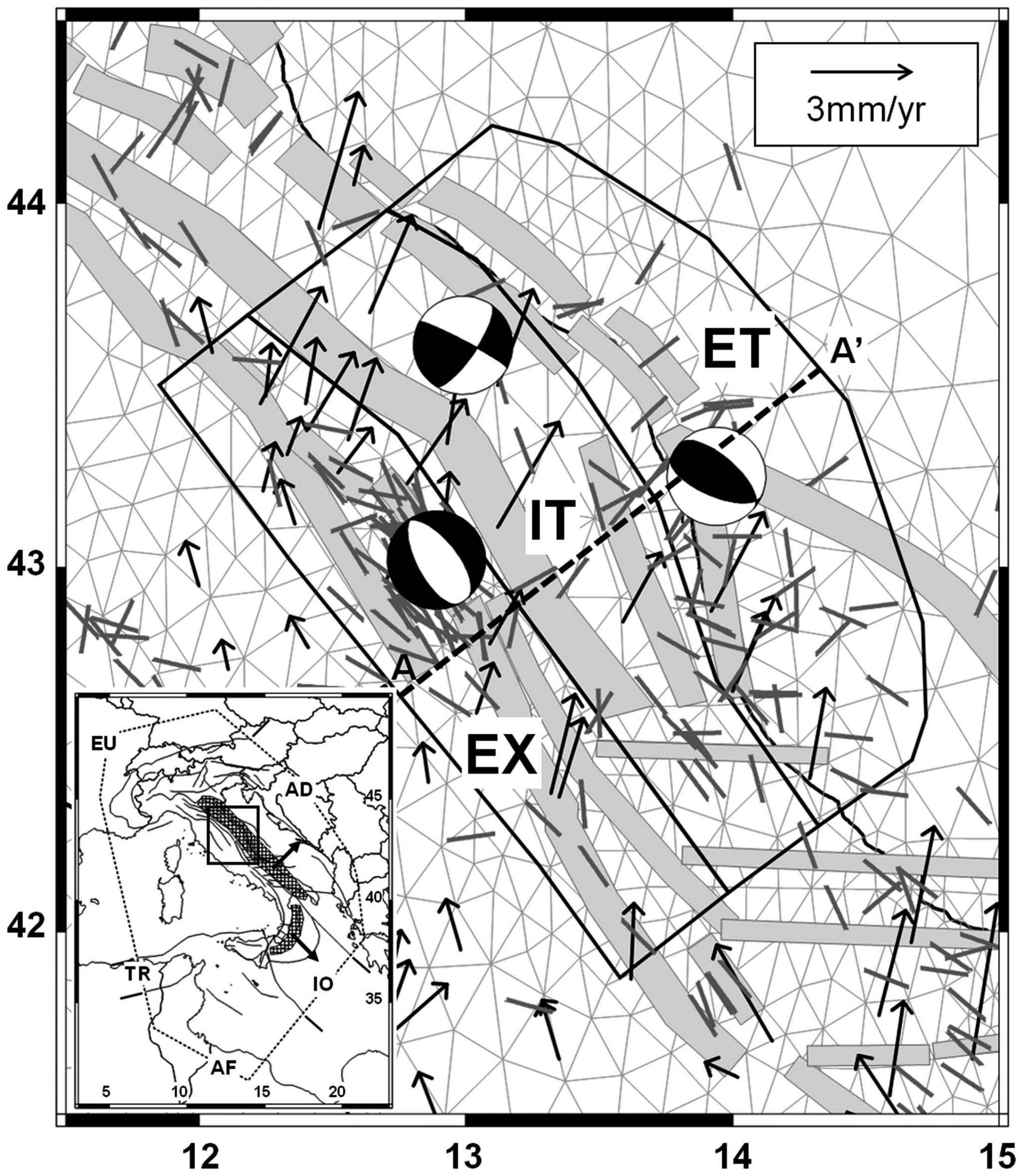
3mm/yr
ET
A'
IT
A
EX
EU
AD
45
40
TR
IO
35
AF
5
10
15
20
44
43
42
12
13
14
15

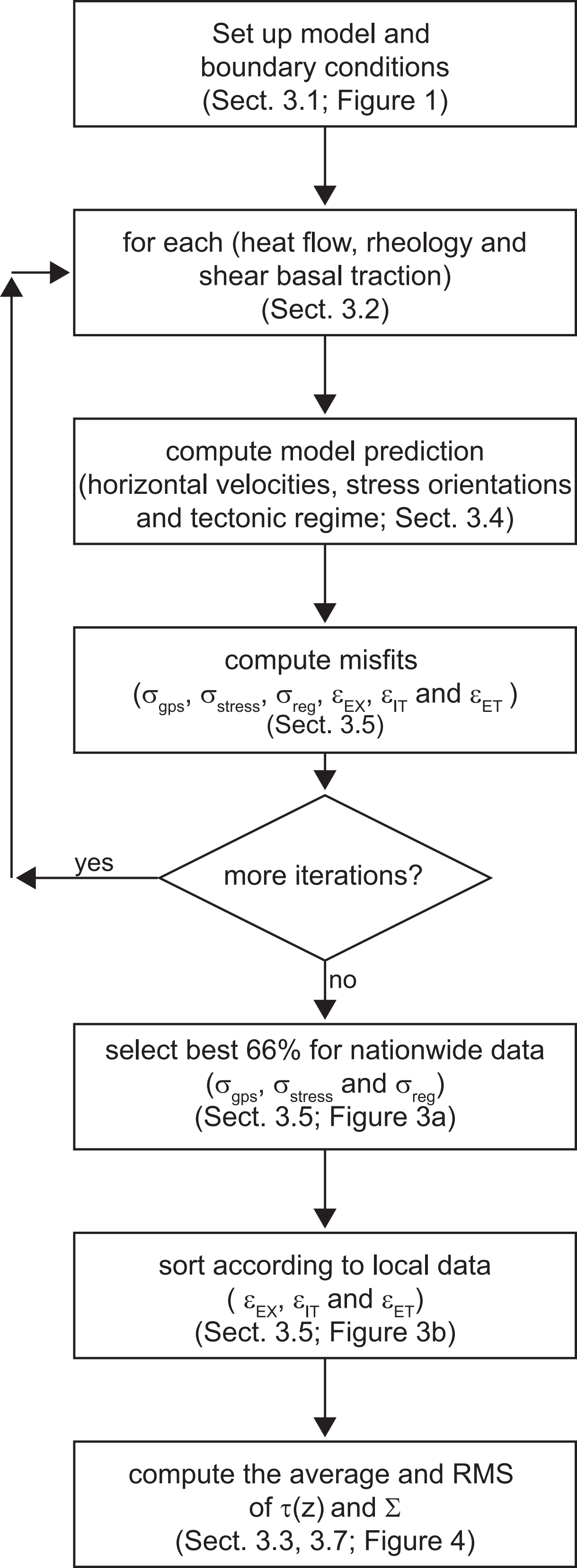
Set up model and boundary conditions (Sect. 3.1; Figure 1)
for each (heat flow, rheology and shear basal traction) (Sect. 3.2)
compute model prediction (horizontal velocities, stress orientations and tectonic regime; Sect. 3.4)
compute misfits (σ_{gps}, σ_{stress}, σ_{reg}, ε_{EX}, ε_{IT} and ε_{ET}) (Sect. 3.5)
more iterations?
yes
no
select best 66% for nationwide data (σ_{gps}, σ_{stress} and σ_{reg}) (Sect. 3.5; Figure 3a)
sort according to local data (ε_{EX}, ε_{IT} and ε_{ET}) (Sect. 3.5; Figure 3b)
compute the average and RMS of $\tau(z)$ and Σ (Sect. 3.3, 3.7; Figure 4)

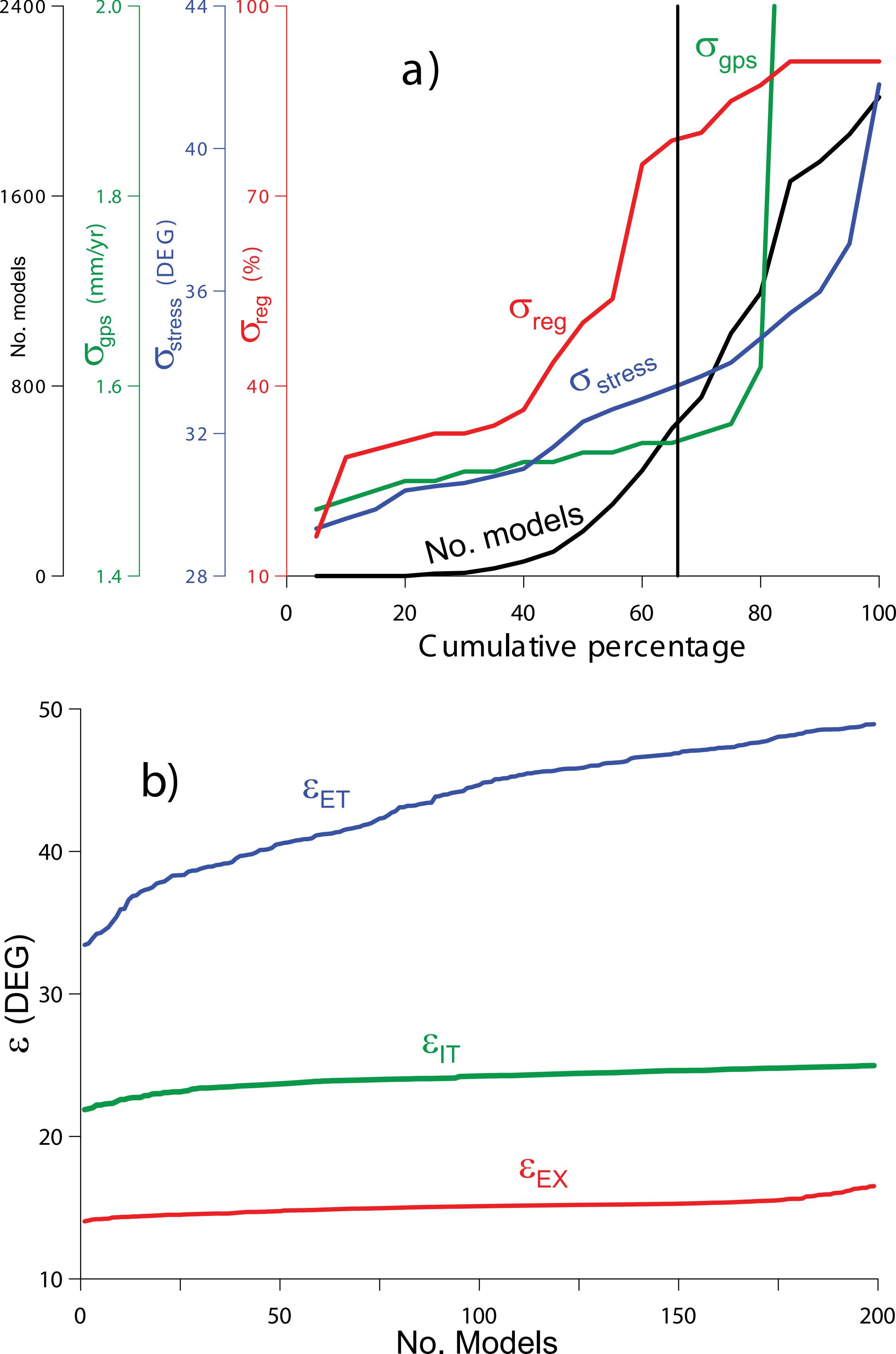

a)
b)
No. models
σ_{gps} (mm/yr)
σ_{stress} (DEG)
σ_{reg} (%)
σ_{gps}
σ_{reg}
σ_{stress}
No. models
Cumulative percentage
ε_{ET}
ε_{IT}
ε_{EX}
ε (DEG)
No. Models

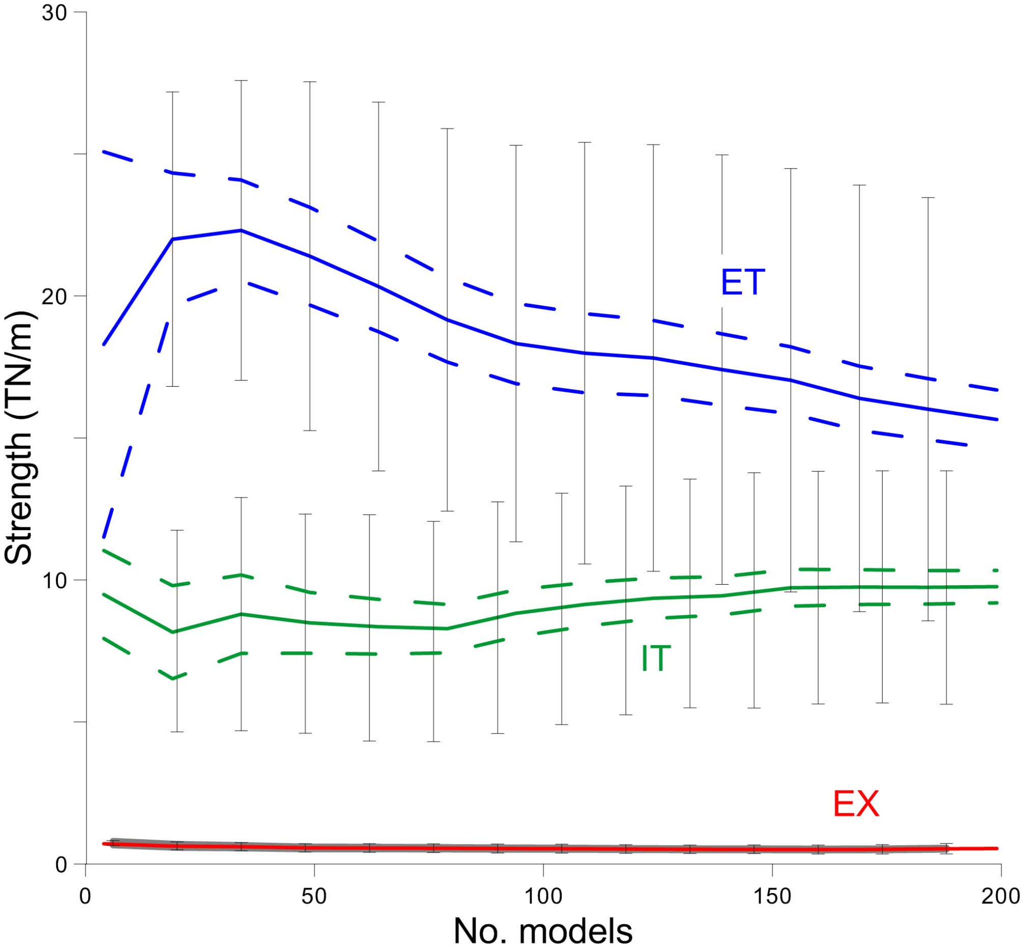

30
20
10
0
Strength (TN/m)
ET
IT
EX
0
50
100
150
200
No. models

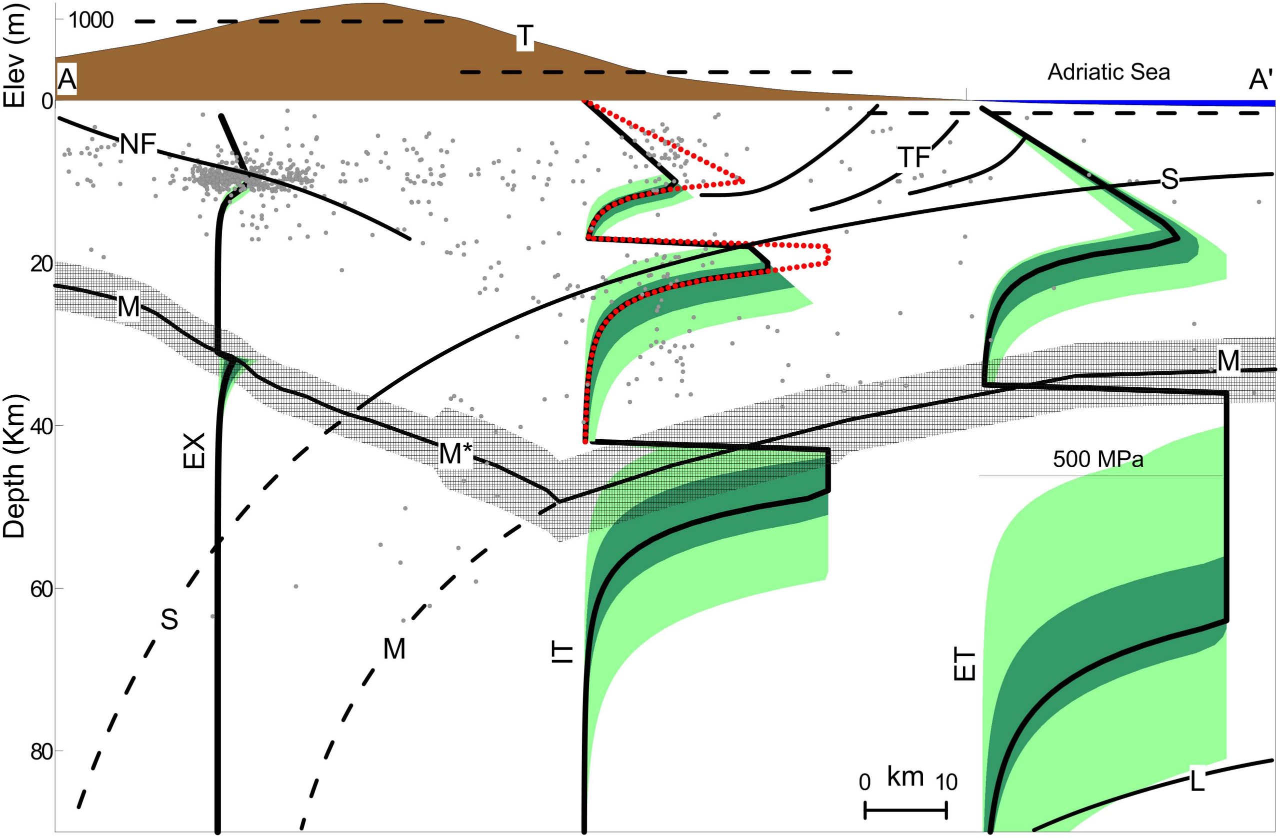

Elev (m)
1000
0
A
T
Adriatic Sea
A'
NF
TF
S
M
M*
EX
S
M
IT
ET
500 MPa
L
0 km 10
Depth (Km)
20
40
60
80

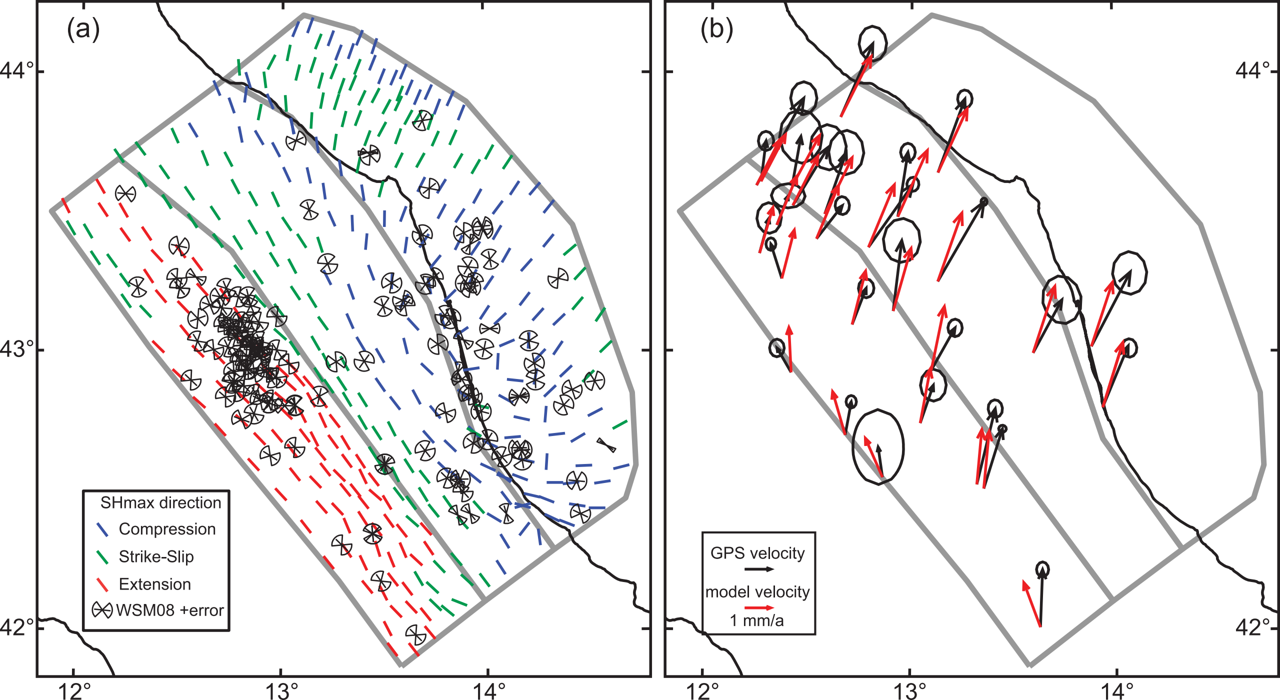
(a)
(b)
44°
43°
42°
12°
13°
14°
SHmax direction
Compression
Strike-Slip
Extension
WSM08 +error
GPS velocity
model velocity
1 mm/a

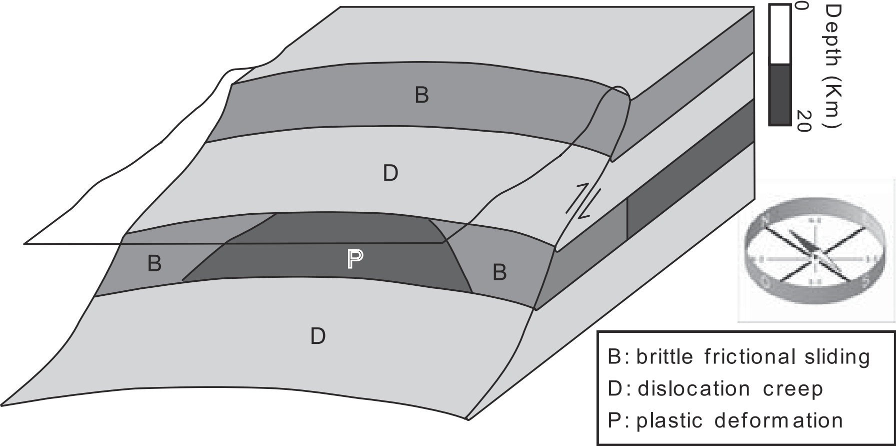

Depth (Km)
0
20
B
D
B
P
B
D
B: brittle frictional sliding
D: dislocation creep
P: plastic deformation